



# A 3D conducting scaffold with in-situ grown lithiophilic Ni<sub>2</sub>P nanoarrays for high stability lithium metal anodes

Huai Jiang<sup>a</sup>, Hailin Fan<sup>a,c</sup>, Zexun Han<sup>a</sup>, Bo Hong<sup>a,\*</sup>, Feixiang Wu<sup>a</sup>, Kai Zhang<sup>a,b</sup>, Zhian Zhang<sup>a</sup>, Jing Fang<sup>a</sup>, Yanqing Lai<sup>a,b,\*</sup>

<sup>a</sup> School of Metallurgy and Environment, Central South University, Changsha 410083, Hunan, China

<sup>b</sup> Engineering Research Centre of Advanced Battery Materials, The Ministry of Education, Changsha 410083, Hunan, China

<sup>c</sup> Contemporary Amperex Technology Co., Ltd., Ningde 352100, Fujian, China

## ARTICLE INFO

### Article history:

Received 25 March 2020

Revised 2 June 2020

Accepted 3 June 2020

Available online 18 June 2020

### Keywords:

Li metal anodes

Ni<sub>2</sub>P nanoarrays

3D metal framework

Uniform Li deposition

Superior lithiophilicity

## ABSTRACT

Lithium (Li) metal is the most potential anode material for the next-generation high-energy rechargeable batteries. However, intrinsic surface unevenness and 'hostless' nature of Li metal induces infinite volume effect and uncontrollable dendrite growth. Herein, we design the in-situ grown lithiophilic Ni<sub>2</sub>P nanoarrays inside nickel foam (PNF). Uniform Ni<sub>2</sub>P nanoarrays coating presents a very low nucleation overpotential, which induces the homogeneous Li deposition in the entire spaces of three-dimensional (3D) metal framework. Specifically, the lithiophilic Ni<sub>2</sub>P nanoarrays possess characteristics of electrical conductivity and structural stability, which have almost no expansion and damage during repeating Li plating/stripping. Therefore, they chronically inhibit the growth of Li dendrites. This results in an outstanding Coulombic efficiency (CE) of 98% at 3 mA cm<sup>-2</sup> and an ultralong cycling life over 2000 cycles with a low overpotential. Consequently, the PNF-Li||LiFePO<sub>4</sub> battery maintains a capacity retention of 95.3% with a stable CE of 99.9% over 500 cycles at 2C.

© 2020 Science Press and Dalian Institute of Chemical Physics, Chinese Academy of Sciences. Published by ELSEVIER B.V. and Science Press. All rights reserved.

## 1. Introduction

With the rapid development and popularity of electronic products, electric vehicle and intermittent power station, economical and high-performance energy storage systems are needed urgently [1,2]. As the most potential anode material of the high-energy rechargeable batteries, Li metal anode with irresistible high theoretical capacity of 3860 mAh g<sup>-1</sup> and the most negative potential (−3.04 V vs. standard hydrogen electrode), has attracted widespread attention [3,4]. However, there are two major problems that hinder its industrial application. One is 'hostless' nature of Li metal, which causes infinite volume change [5]; the other is inhomogeneous lithium deposition, accompanying by the growth of Li dendrites [6,7]. These are the main reasons why Li metal batteries have shown low Coulombic efficiency, fast capacity decay, high safety risk and been far from the practical application.

To address these intractable problems, various ingenious strategies have been taken. These strategies include optimizing

the electrolytes and additives [8–10], solid state electrolytes [11], artificial SEI layers or physical protection layers [7,12], mechanical surface modification of Li foils [13], 3D printing [14], and regulating the construct of Li metal anodes [15]. Though Li metal anodes are effectively stabilized by these modified strategies, yet the inevitable volume change is difficult to overcome due to the SEI layers being insufficiently robust during the Li plating/stripping. Sand's time model [16] clarifies the inversely proportional relationship between the time when Li dendrites begin to grow and current density under the cell polarizations. Therefore, 3D frameworks with high specific surface area and excellent structural stability have been considered as an ideal approach to uniform Li plating/stripping [17]. Based on above theoretical analysis, all kinds of novel 3D frameworks, such as hollow carbon spheres [18], carbon nanotubes [15], graphene-based 3D skeletons [19,20], porous carbon film [21], polyimide nanofabric [22] and porous 3D nickel [23], have been verified.

Benefiting from 3D interconnected porous construction with good performance of electrical conductivity and mechanical property, commercial metal current collectors, such as copper (Cu) and nickel (Ni) foam, have been widely applied to electrocatalysis [24], supercapacitors [25] and batteries [26]. In practice, cost-efficient

\* Corresponding authors at: School of Metallurgy and Environment, Central South University, Changsha 410083, Hunan, China.

E-mail addresses: [bop\\_hong@csu.edu.cn](mailto:bop_hong@csu.edu.cn) (B. Hong), [laiyanqing@csu.edu.cn](mailto:laiyanqing@csu.edu.cn) (Y. Lai).

porous metal foam could be ideally applied as the host of Li metal anode due to its mass production and extendibility features [27,28]. However, due to 'lithiophobic' nature and heterogeneity of metal foams inducing uneven transportation of Li-ion flux, Li would prefer to plate on the tip or the edge of metallic skeletons where the electrons can be accepted easily, resulting in a lot of space not being fully utilized and uncontrollable dendritic Li formation [29]. Especially, Li dendrite growth is further exacerbated because of high nucleation barrier under a high current density [30]. Fortunately, the surface lithiophilic modification of metal framework is a practical solution to solve this dilemma. Several materials such as precious metal Au [31], Ag [32], transition metal oxides ( $\text{Cu}_2\text{O}$  [33],  $\text{ZnO}$  [34,35],  $\text{CoO}$  [36]), metal sulfides ( $\text{Cu}_2\text{S}$  [37]), metallic nitrides ( $\text{Ni}_3\text{N}$  [38]) with lithiophilic feature have been studied. However, the metallic lithiophilicity materials are easily to cause structural expansion and collapse due to alloying and de-alloying with Li metal during the repetitious charge/discharge under high current density [39,40]. Other lithiophilic materials, on the other hand, easily increase polarization due to their poor electrical conductivity. Therefore, it is necessary to find a lithiophilic material with good conductivity and structural stability.

Here, we propose a lithiophilic material of nickel phosphide ( $\text{Ni}_2\text{P}$ ) that performs superior characteristics of conductivity and structural stability during repeated Li plating/stripping. Furthermore, given the metallic Li plating/stripping behavior interrelating with surface morphology of substrates [41–43], we design in-situ grown lithiophilic  $\text{Ni}_2\text{P}$  nanoarrays inside nickel foam (PNF) through a simple hydrothermal-phosphating two-step procedure (Fig. 1a). Surprisingly, the PNF exhibits multiple benefits relative to the bare nickel foam (NF): (1) High specific surface area, effectively reducing the local current density, homogenizing Li-ion flux, and regulating Li-ion distribution on the skeleton surface; (2) the uniform 3D lithiophilic structure reducing the overpotential for lithium plating, in favor of homogeneous lithium deposition; (3) a stable lithiophilic skeleton to eliminate volume change and form a uniform and robust SEI. In addition, these advantages of facile preparation condition and economical performance will be beneficial to turn the commercial Ni foam into high-performance Li-host, promoting the practical applications of Li metal anodes. Therefore, this specially constructed metal current collector (PNF) achieves a high Coulombic efficiency of 98% over 210 cycles at  $3 \text{ mA cm}^{-2}$  for half-cell, and even exhibits a long lifespan of 2100 h over 2000 cycles with a low voltage hysteresis at  $2 \text{ mA cm}^{-2}$  for symmetric cell.

## 2. Results and discussion

PNF has been realized by a universal two-step process as shown in Fig. 1(a). The hydrothermal treatment could wipe off surface impurity and grease of NF (Fig. 2a). The surface of NF is corroded by the low concentrations of hydrofluoric acid dilute solution etching (Fig. 2b), but the phase of etching Ni foam (HNF) is still nickel (Fig. 2d). Subsequently, HNF is phosphatized with decomposed  $\text{NaH}_2\text{PO}_4 \cdot \text{H}_2\text{O}$  under  $350^\circ\text{C}$  by gas–solid reaction process with a certain heating rate and ventilation rate to achieve PNF, whose surface is decorated with  $\text{Ni}_2\text{P}$  nanoarrays (Fig. 2c). Thus, phosphating is applied to transform HNF to PNF. The peaks of  $\text{Ni}_2\text{P}$  are clearly showed in the XRD pattern (Fig. 2d). The energy-dispersive X-ray spectroscopy (EDX) mapping of PNF reveals that elements of nickel and phosphorus are evenly distributed on the surface of metal skeleton (Fig. 2e). The atomic ratio of Ni and P from EDX is 66.9:33.1, which is close to the ratio of XRD result. It indicates that lithiophilic  $\text{Ni}_2\text{P}$  nanoarrays in situ grow inside Ni foam. Brunauer-Emmett-Teller (BET) test (Fig. S1) has proved that PNF is rough

enough to enable lower local current density. The chemical composition and valence of PNF are accurately characterized by X-ray photoelectron spectroscopy (XPS). XPS survey demonstrates the presence of Ni and P. The high-resolution XPS spectrum of Ni 2p can be deconvoluted into eight subpeaks (Fig. 2f). The peaks at 852.6 and 869.85 eV correspond to the Ni  $2p_{3/2}$  and Ni  $2p_{1/2}$  of Ni – P, which verify the presence of  $\text{Ni}^+$ . The peaks at 856.5 and 874.5 eV relate to the Ni  $2p_{3/2}$  and Ni  $2p_{1/2}$  of Ni – O, which verify the presence of  $\text{Ni}^{2+}$ . In addition, because of the shakeup excitation of the high-spin  $\text{Ni}^{2+}$ , another four satellite peaks are found in 860.35, 862.9, 874.5 and 880.9 eV [44]. The high-resolution spectrum of P 2p (Fig. 2g) reveals the existence of P  $2p_{3/2}$  at 129.46 eV and P  $2p_{1/2}$  at 130.27 eV, which correspond with the chemical bond between P and Ni. Another peak at around 134.31 eV can be attributed to the oxidized phosphate species. To preliminarily forecast the lithiophilicity of  $\text{Ni}_2\text{P}$  and related products, the binding energies ( $E_b$ ) of a lithium atom with different substrates were estimated by density functional theory (DFT) calculations (Fig. 1b and c). The optimal Li adsorption on the thermodynamically stable surface of Ni (111) (Fig. S2a),  $\text{Ni}_2\text{P}$  (001) (Fig. 1b),  $E_b$  is  $-2.118$  and  $-2.886$  eV (Fig. 1c), respectively. The reaction between the  $\text{Li}^+$  and the  $\text{Ni}_2\text{P}$  in-situ generates passivation layer containing  $\text{Li}_3\text{P}$  [44,45]. The  $E_b$  of subsequent Li adsorption on  $\text{Li}_3\text{P}$  (001) (Fig. S2b) reaches up to  $-9.47$  eV, which shows excellent lithiophilicity. To intuitively test lithiophilicity of PNF host, wettability experiments of molten Li onto various substrates were conducted. In the first second, the PNF is quickly wetted when contacting with molten Li. After 90 sec, the molten Li is successfully infused in the PNF host (Fig. 1e), which shows the PNF possessing fine Li affinity. Conversely, the contact angles of molten Li on NF are always large throughout the process (Fig. 1d), which presents a poor wettability of NF. These simulation and wettability results indicate the better lithiophilicity of PNF, which will be beneficial to uniform nucleation and deposition of Li metal into 3D conducting scaffold.

Furthermore, the morphology evolution process of PNF has been studied at various concentrations of HF, heating rates and ventilation rates of phosphating by a series of comparative experiments. When NF is treated by hydrothermal at 0.3 wt% HF, the surface of HNF is uniform and rough. Subsequently,  $\text{Ni}_2\text{P}$  nanoarrays is achieved by phosphating. However, the morphologies and structures of HNF present excessive corrosion (Fig. S3a) or under-reaction (Fig. S3c) under other concentrations of HF and uniform  $\text{Ni}_2\text{P}$  nanoarrays fail to be fabricated. In addition, the heating rate of phosphating has great effect on  $\text{Ni}_2\text{P}$  layer's morphology (Fig. S5). Perfect PNF (Fig. S5b) is obtained by phosphating 0.3 wt % HF treated HNF, under a controlled phosphating heating rate,  $1^\circ\text{C/min}$ . In contrast, if heating rates of phosphating are lower (Fig. S5a) or higher (Fig. S5c), the uniform lithiophilic  $\text{Ni}_2\text{P}$  nanoarrays cannot be achieved. Besides, the ventilation rate of phosphating is also the key factor to morphology evolution of PNF (Fig. S7). When ventilation rate of  $\text{Ar}/\text{H}_2$  from 40 mL/min increases to 160 mL/min,  $\text{Ni}_2\text{P}$  layer's morphology transforms from punctiform  $\text{Ni}_2\text{P}$  (Fig. S7a), uneven  $\text{Ni}_2\text{P}$  (Fig. S7b), lamellar  $\text{Ni}_2\text{P}$  (Fig. S7c) to the lithiophilic  $\text{Ni}_2\text{P}$  nanoarrays (Fig. S7d). The thickness of  $\text{Ni}_2\text{P}$  layer is about only 4.62  $\mu\text{m}$ , which shows good homogeneity (Fig. S9). It reveals that relatively high speed  $\text{Ar}/\text{H}_2$  is beneficial to form the uniform structure of lithiophilic  $\text{Ni}_2\text{P}$  nanoarrays.

The Coulombic efficiency (CE) is an important indicator to evaluate the sustainability of lithium anodes. To explore the electrochemical performance of PNF under different preparation conditions, coin half cells were assembled with lithium foil as the counter electrode and PNF as the working electrode to study their CEs and cycling abilities at  $3 \text{ mA cm}^{-2}$  for  $1 \text{ mAh cm}^{-2}$ . For PNF produced by HNF with different concentrations of HF, we test the different CEs (Fig. S4), whose results show that the samples

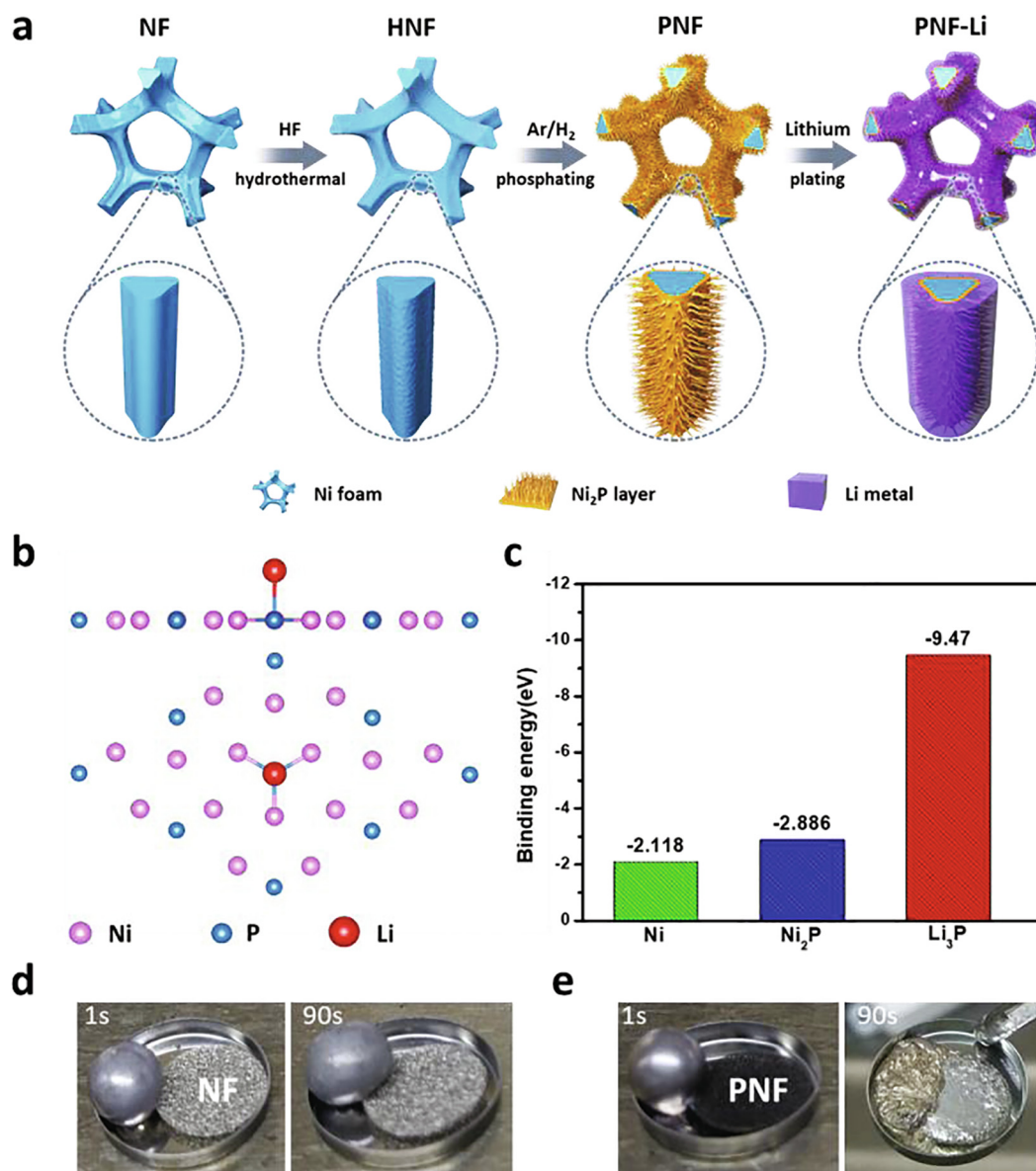


**Fig. 1.** (a) Schematic of the preparation process of PNF. (b) Calculated binding energies of a Li atom with Ni<sub>2</sub>P substrate by DFT, here the pink, blue and red spheres represent Ni, P and Li atoms respectively. (c) Binding energies comparison of a Li atom with Ni, Ni<sub>2</sub>P and Li<sub>3</sub>P. Wettability of molten Li onto various substrates: (d) bare Ni foam; (e) PNF.

under concentration of 0.3 wt% HF realize the best cyclic stability due to perfect lithiophilic Ni<sub>2</sub>P nanoarrays and abundant lithiophilic sites. When NF is etched by 0.3 wt% HF, subsequently, the samples of PNF are achieved by different heating rates of phosphating under the same ventilation rate. The CEs of these samples show 1 °C/min achieves higher CE relative to that of 0.5 and 2 °C/min (Fig. S6). On this basis, the nanoarrays structure of Ni<sub>2</sub>P is fabricated under the ventilation rate of 160 mL/min, whose CE is the highest compared with the lower ventilation rate (Fig. S8). It reveals that the lithiophilic Ni<sub>2</sub>P nanoarrays modified Ni foam is fabricated and possesses the best electrochemical performance under 0.3 wt% HF etched, 1 °C/min of heating rate and the ventilation rate of 160 mL/min. The lower lithium nucleation overpotential and polarization will be beneficial to uniform deposition of Li metal during Li<sup>+</sup> reduction process [18,46]. Fig. 3(a) shows lithium nucleation behavior at a current density of 0.5 mA cm<sup>-2</sup> with a capacity of 2 mAh cm<sup>-2</sup> during the first deposition process. At the beginning of the deposition, there is obvious voltage drop for NF, HNF and PNF, about -115, -176.4 and -29.1 mV,

respectively. With the continuous deposition of Li metal, the curve gradually rises into a platform, which represents polarization voltages. PNF exhibits a lower polarization (-14.9 mV) than that on the NF (-27 mV) and the HNF (-38.4 mV), which means Li-ion has lower interface impedance in the process of transferring from electrolyte to the surface of PNF. Therefore, the lower nucleation overpotential of PNF (14.2 mV) has been achieved due to the outstanding lithiophilicity. The poor lithiophilicity of NF and the non-uniform surface of HNF result in a large nucleation overpotential of 88.0 and 138 mV, respectively. Fig. 3(d) shows the CEs of NF, HNF and PNF at a current density of 3 mA cm<sup>-2</sup> with a capacity of 1 mAh cm<sup>-2</sup>. The CEs of NF and HNF rapidly decline after 60 and 34 cycles, respectively. In contrast, the PNF maintains stable after 210 cycles with a high CE of 98%. As current density rises to 5 mA cm<sup>-2</sup> (Fig. 3e), the PNF keeps stable for more than 160 cycles and the CE value is as high as 98.3%. However, the CE values of NF and HNF are unstable and decay gradually after 30 cycles. Further increasing the current density to 8 mA cm<sup>-2</sup> (Fig. 3f), the PNF remains steady for more than 128 cycles with a CE value of 95.7%, but the average CEs



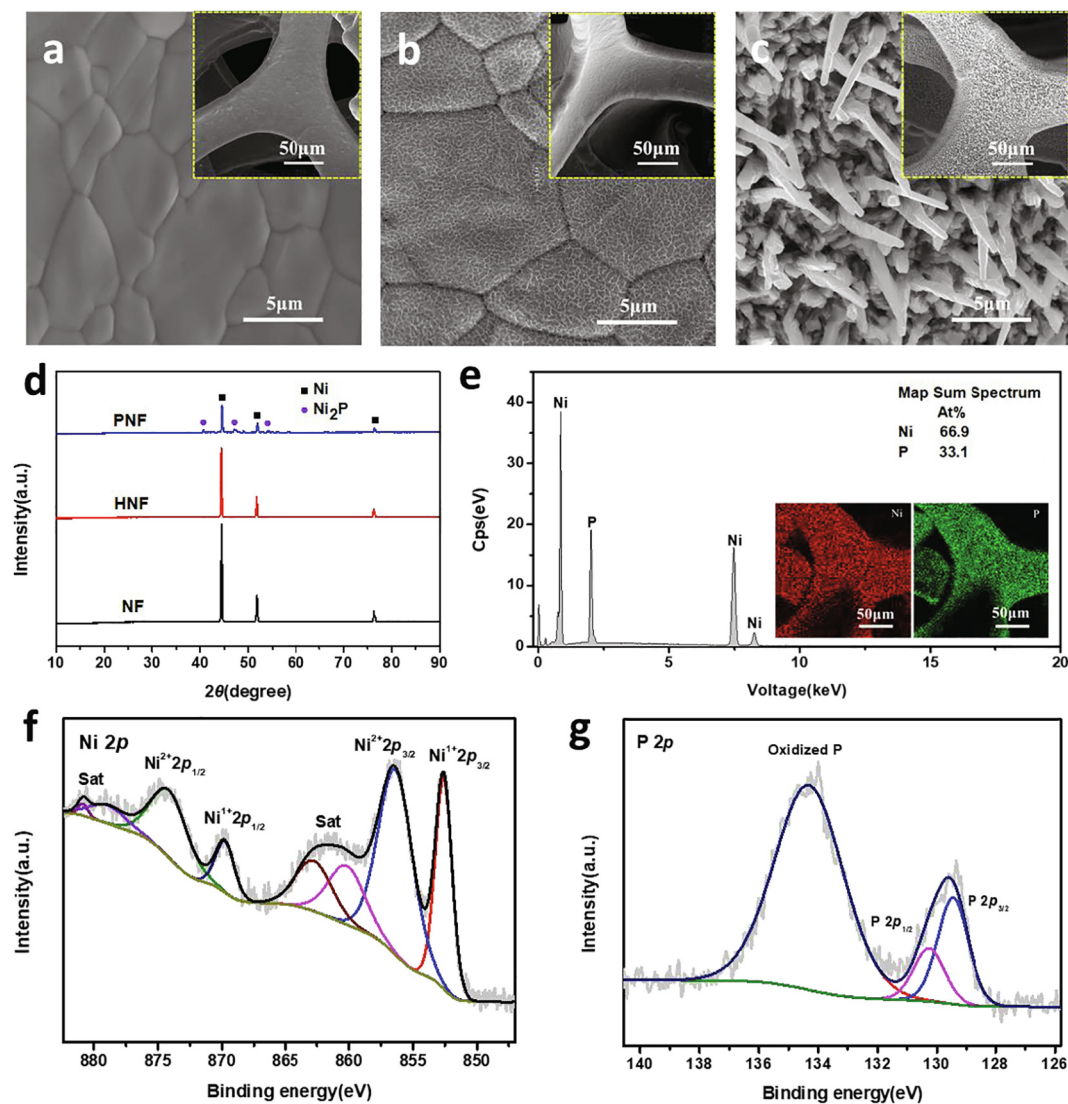
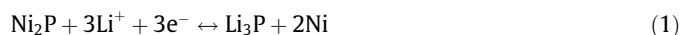


**Fig. 2.** Characterization of NF, HNF and PNF. SEM images of the (a) bare Ni foam (NF), (b) hydrofluoric acid dilute solution etching Ni foam (HNF) and (c) PNF. (d) XRD patterns of NF, HNF and PNF. (e) EDX spectrograms of PNF and corresponding elemental mapping images of Ni and P. XPS spectra of the PNF of (f) Ni 2p and (g) P 2p.

of NF and HNF only keep 90.7%, 85.9% in 66 cycles and 49 cycles. As we all known, Li-ion concentration distribution is not uniform in Li metal batteries. As Fig. 3(g) shows, Li metal tends to deposit on bare Ni foam/separators interfaces where Li-ion capture electrons quickly, which leads to insufficient utilization of the interior voids and growth of Li dendrites or even short circuits during repeating plating/stripping. This is the key reason that NF and HNF electrodes present the low CE and poor sustainability. However, it is clear that PNF electrode realizes stable CE, and maintains high reversibility at the high current density. The unique 3D Ni<sub>2</sub>P nanoarrays structure maximizes specific surface area of electrode, which will effectively reduce local current density. Furthermore, the lithiophilic Ni<sub>2</sub>P nanoarrays reduce nucleation overpotential and ensure uniform Li deposition, while the poor lithiophilicity of HNF electrode leads to a low CE. In addition, on the surface of the Ni<sub>2</sub>P layer, the reaction between the Li and Ni<sub>2</sub>P in-situ formed the highly Li<sup>+</sup>-conducting Li<sub>3</sub>P ( $\approx 10^{-4}$  S cm<sup>-1</sup>) [47], which further provides a better lithiophilic interface conducting fast and uniform transfer of ions. The in-situ formed nano Ni is electron-conducting carrier that enhances the kinetics of electrode [48]. As a result, Li metal is evenly dispersed on the surface of PNF skeleton, inhibiting Li dendrite formation (Fig. 3h).

Fig. 3(b and c) show the voltage–capacity curves of PNF and NF electrodes in different cycles at a current density of 3 mA cm<sup>-2</sup> with a capacity of 1 mAh cm<sup>-2</sup>. The electrochemical behavior of PNF (Fig. 3b) during Li deposition process can be divided into two stages. The first stage is the lithiation of Ni<sub>2</sub>P, similar to the activation process of the substrate (Fig. S17a). Combined with CV curves (Fig. S10), the peak (~1.28 V) indicates the reaction [45] between the Li<sup>+</sup> and the Ni<sub>2</sub>P layer is as follows:



Another reduction peak at ~0.51 V is owing to the generation of amorphous Li<sub>3</sub>P and solid electrolyte interface (SEI) film. XPS of P 2p after the 1st and 50th stripping is showed in Fig. S11. Li<sub>3</sub>P and LiP are confirmed by the peaks at 129.14 and 130.14 eV, respectively [49,50]. LiP is the product of Li<sub>3</sub>P decomposition by a secondary reversible reaction. In addition, the peaks at 133.04 and 134.04 eV reveal the existence of phosphate which is originated from the inevitable exposure with air [51]. The in-situ formed LiP/Li<sub>3</sub>P, as the component of SEI layer, acts as passivation layer (Fig. S12), preventing side reactions between Li and electrolyte, thus suppressing Li dendrite growth. At the second stage, when the voltage continues to drop below 0 V, the product layer

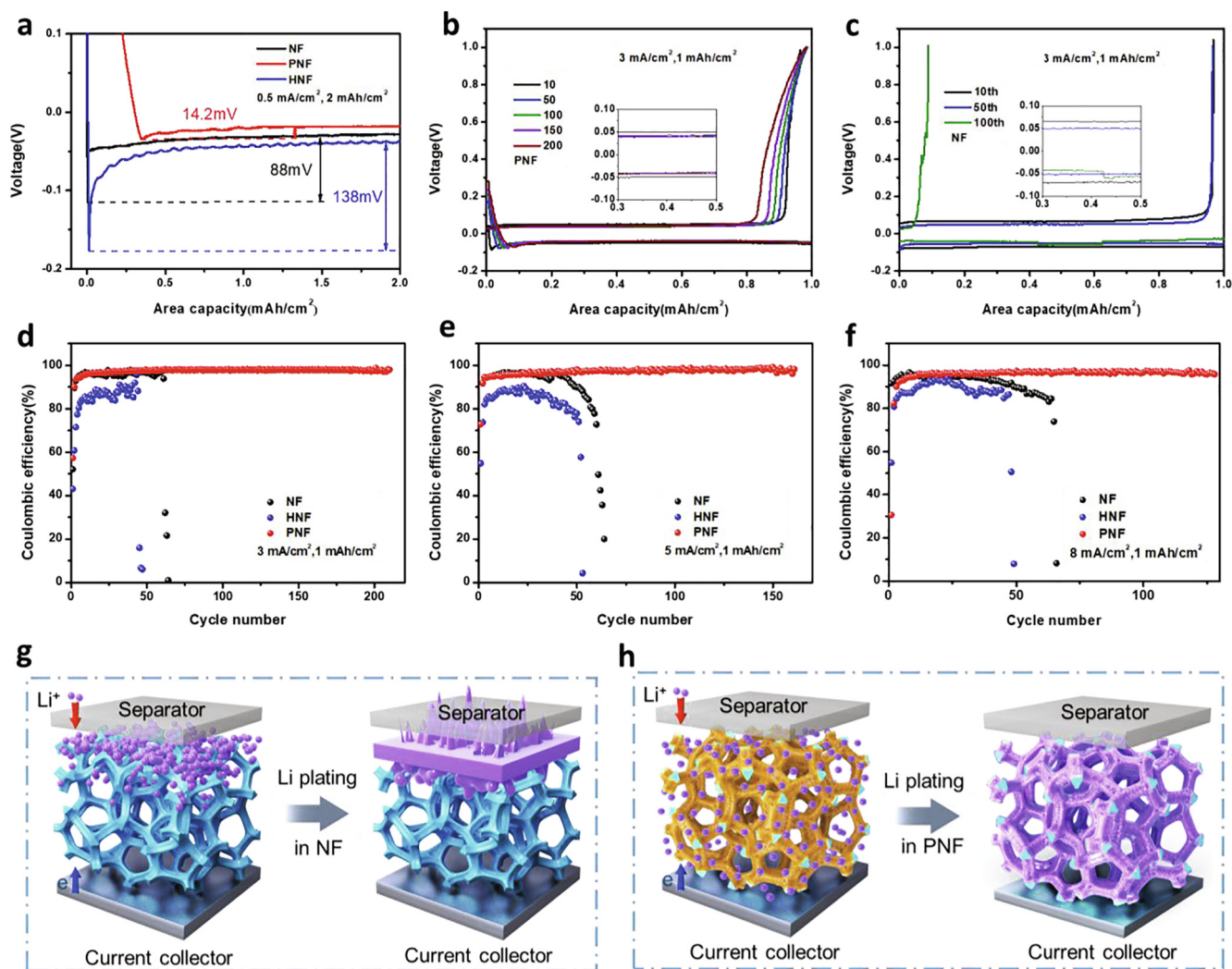


**Fig. 3.** Electrochemical performance of PNF and Li deposition mechanism. (a) The voltage–capacity curves of the lithium nucleation process at 0.5 mA cm<sup>-2</sup>. Voltage profiles for (b) PNF and (c) NF with a current density of 3 mA cm<sup>-2</sup>. Coulombic efficiencies of NF, HNF and PNF at different current densities with a total capacity of 1 mAh cm<sup>-2</sup>: (d) 3 mA cm<sup>-2</sup>, (e) 5 mA cm<sup>-2</sup> and (f) 8 mA cm<sup>-2</sup>. Li deposition mechanism on different substrates: (g) NF and (h) PNF.

containing LiP/Li<sub>3</sub>P provides more sites of Li nucleation and induces Li deposition on it (Fig. S17b), which contributes to gradually weakening the reaction between Li and Ni<sub>2</sub>P layer. Ex situ XRD patterns of the PNF electrode at the charge/discharge states further proof the invertibility of the reaction (1) and the structure of lithiophilic Ni<sub>2</sub>P nanoarrays can remain stably (Fig. S13). Li metal uniformly plates on the surface of PNF. Except for 10th cycles, PNF electrode displays low polarization voltage hysteresis of 40 mV in 200 cycles. In contrary, NF electrode is less stable and presents higher polarization voltage of over 50 mV, due to much ‘dead lithium’ formation at 100th cycle (Fig. 3c). The EIS results (Fig. S14) certify that PNF electrode has lower charge-transfer resistance, showing stable electrode/electrolyte interface and superior Li plating/stripping kinetics. However, the EIS results of NF electrode are always fluctuating and display poor stability of interface after continuous cycling due to a mount of ‘dead lithium’ accumulation. So, the lower polarization voltage of PNF electrode is attributed to Ni<sub>2</sub>P with metalloid characteristics and superior conductivity [52,53]. In-situ formation of protective layer containing LiP/Li<sub>3</sub>P, on the other hand, homogenizes Li-ion flux [54], resulting in lower interface impedance.

In order to intuitively understand the behavior of Li plating/stripping, PNF and NF electrodes were used in comparative study

at a current density of 3 mA cm<sup>-2</sup> with a capacity of 1 mAh cm<sup>-2</sup> by assembling coin half cells. It is seen that lots of granular lithium (Fig. 4b) unevenly deposits on the smooth surface of NF (Fig. 4a), while metallic Li can be deposited on lithiophilic Ni<sub>2</sub>P nanoarrays (Fig. 4e), and finally uniformly fills the entire skeleton surface of the PNF (Fig. 4f) in the 1st cycle. And then, much mossy Li (Fig. 4j) is left on the NF surface (Fig. 4i) after stripping, while Li is stripped completely on the PNF surface (Fig. 4n) compared with the pristine (Fig. 4m). With continuous plating/stripping, Li exhibits dendritic deposition on NF (Fig. 4c), and noodle-like dead lithium remains on the edge of NF skeleton after the 50th stripping (Fig. 4k). When the coin cell runs for 100 cycles, inhomogeneous Li metal deposition becomes much worse (Fig. 4d), and massive blocky dead lithium accumulates on NF surface after stripping (Fig. 4l). Considering the features of NF, Li tends to preferentially deposit on the place where electrons are easier to get, which will result in uneven lithium nucleation and Li-ion flux distributing [55], finally promoting the formation of Li dendrites. Quite differently, Li uniformly deposits on the surface of the PNF without Li dendrites (Fig. 4g and h). The surface of the PNF gets clean again and lithiophilic Ni<sub>2</sub>P nanoarrays re-expose clearly when Li is stripped (Fig. 4o–p). It indicates that PNF can effectively suppress Li dendrites, and obtain uniform Li plating/stripping. The

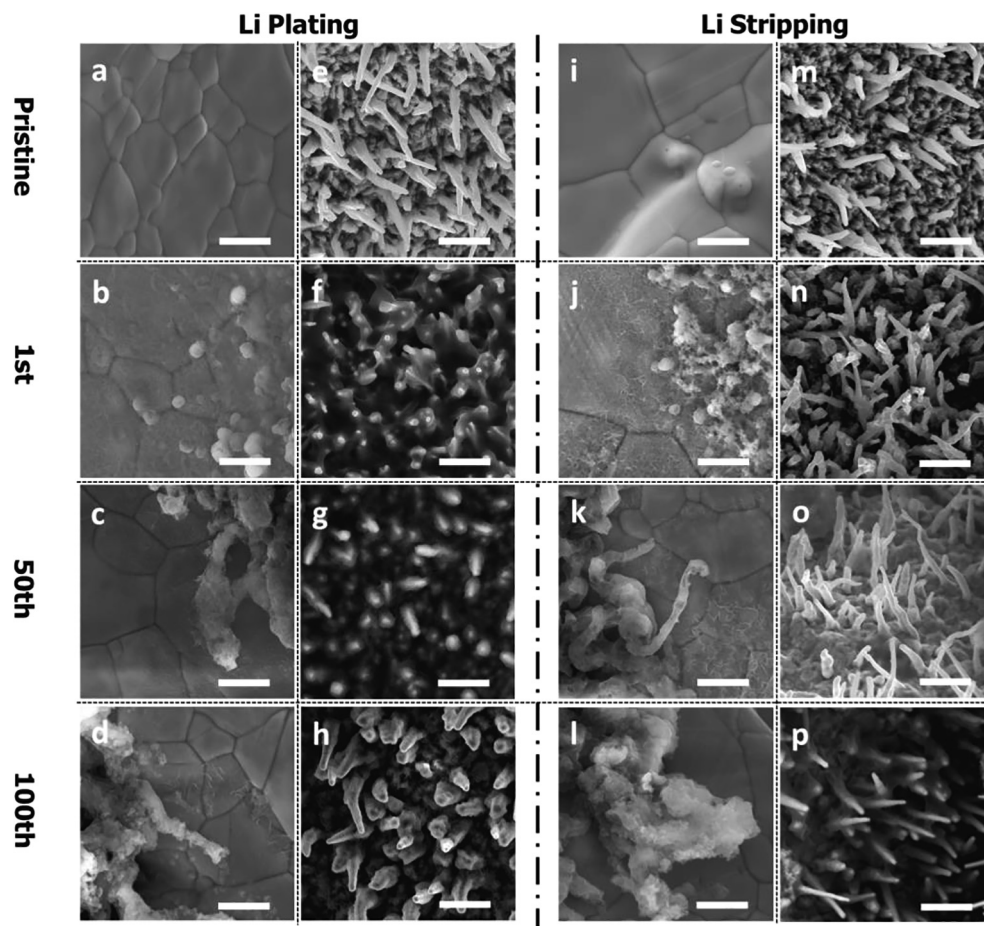


**Fig. 4.** SEM images of Li plating/stripping on NF and PNF with a current density of 3 mA/cm<sup>2</sup> for a total capacity of 1 mAh cm<sup>-2</sup>. The Surface morphology of the original NF (a, i) and PNF (e, m); Li metal morphologies of NF (b–d) and PNF (f–h) after the 1st, 50th and 100th plating, respectively; Li metal morphologies of NF (j–l) and PNF (n–p) after the 1st, 50th and 100th stripping, respectively. The scale bars in (a–p) are 5 μm.

fundamental reasons caused the different Li plating/stripping behaviors are rich specific surface area and ideal lithiophilicity of PNF. These features effectively reduce local current density and provide a large number of Li nucleation sites. In addition, the in-situ formed Li<sub>3</sub>P is one of the fast Li-ion conductors, which reduces the interface impedance and promotes the electrochemical kinetics. These advantages improve the uniformity of the Li-ion flux distribution [56], which achieves uniform Li plating/stripping on lithiophilic Ni<sub>2</sub>P nanoarrays modified Ni foam.

To further demonstrate that the lithiophilic Ni<sub>2</sub>P nanoarrays could significantly induce Li plating evenly, Li metal with different capacities was electroplated on the substrates (PNF and NF) at a current density of 1 mA cm<sup>-2</sup> (Fig. 5). When the NF electrode is plated with 3 mAh cm<sup>-2</sup>, Li tends to deposit locally (Fig. 5a). With increasing the plating capacity of Li to 5, 8 and 15 mAh cm<sup>-2</sup>, moss Li and cotton-like Li dendrite formed, covering the upper surface of the NF (Fig. 5b–d, respectively). Inversely, Li metal is uniformly deposited on the skeleton of PNF, and then always maintaining homogeneous and compact deposition morphology under the different capacities (Fig. 5e–h). It reflects that NF host has the poor affinity for Li, which exacerbates the polarization of electrode, resulting in lithium preferential nucleation and growth on protrusion of skeleton. Different Li deposition behaviors are reflected on the volume change by the cross-section images of NF and PNF. No obvious volume effect shows on the thickness of PNF electrode (150 μm) (Fig. 5m–p), while the thickness of NF electrode increases from 160, 200, 210 to 220 μm (Fig. 5i–l) under a capacity of 3, 5, 8

and 15 mAh cm<sup>-2</sup>, respectively. In Fig. 5(j), fluffy Li metal exposes to the upper surface of NF electrode, while Li metal is well-distributed on the PNF electrode (Fig. 5n). With capacity increasing to 8 mAh cm<sup>-2</sup>, the phenomenon of spatially heterogeneous lithium deposition further worsening, there is obvious stratification for Li metal deposited in 3D framework of NF (Fig. 5k). When the capacity increases to 15 mAh cm<sup>-2</sup>, a thick Li layer covers on the NF substrate (Fig. 5l), while there is no Li metal accumulation on surface of PNF substrate (Fig. 5p) due to perfect lithiophilicity and stable structure. Shorter diffusion path of Li-ion and easier degree of acceptance of the electrons enable Lithium to deposit and grow on the separator-facing surface of the lithiophobic NF. This non-uniform deposition of lithium decreases the utilization of the interior voids and accelerates the degradation of NF electrode during the repeated charge/discharge cycles. In a sharp contrast, Li metal evenly nucleates on lithiophilic Ni<sub>2</sub>P nanoarrays modified NF skeleton due to low nucleation energy barrier. Furthermore, because of in-situ generating protective layer containing Li<sub>3</sub>P, Li metal continuously and homogeneously plates on the PNF electrode.

The symmetric cell is used to evaluate the long-term stability of different electrodes. As can be seen in Fig. 6(a), the bare Li foil electrode presents high overpotential and then the voltage rapidly declines around 150 h, possibly due to Li dendrite-induced short circuit. Similarly, the NF electrode exhibits obvious volatility of the voltage and then sharp rises after 40 h. By contrast, the PNF electrode shows a stable voltage profile with a low overpotential



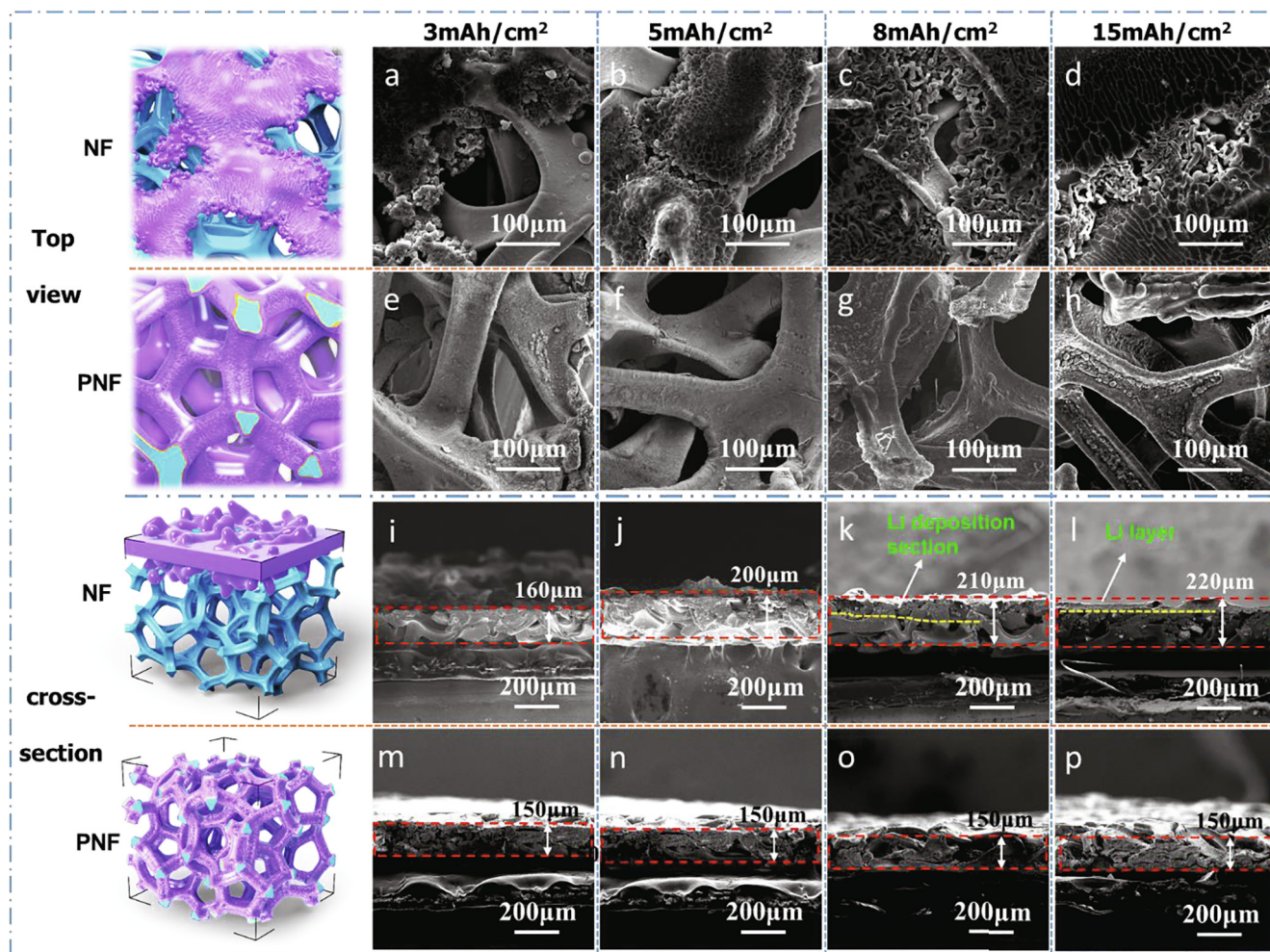


**Fig. 5.** Top-view and cross-section SEM images of NF and PNF deposited with different area capacity lithium at the current density of  $1 \text{ mA cm}^{-2}$ ; Top-view SEM images of NF (a–d) and PNF (e–h) electrode with 3, 5, 8 and  $15 \text{ mAh cm}^{-2}$ , respectively; Cross-section SEM images of NF (i–l) and PNF (m–p) electrode with 3, 5, 8 and  $15 \text{ mAh cm}^{-2}$ , respectively.

and ultralong cycling life of 2100 h over 2000 cycles. With current density further increasing to  $5 \text{ mA cm}^{-2}$  (Fig. 6b), the PNF electrode maintains a relatively stable cycling of 120 cycles with a low voltage hysteresis, while the NF and bare Li foil electrodes display poor cycling and high overpotential. Compared with other modified metal current collectors (Table S1), the outstanding electrochemical cycling performances benefit from the better stability of lithiophilic structure, the more robust SEI layer and lower Li ionic transport resistance of the PNF electrode. In order to further explore the potential application of PNF,  $\text{LiFePO}_4$  as the cathode and Li deposited PNF or NF ( $15 \text{ mAh cm}^{-2}$ ) as the anode were assembled to full cell. As shown in Fig. 6(c), the full cell of PNF-Li|| $\text{LiFePO}_4$  displays superior cycling stability than NF-Li|| $\text{LiFePO}_4$  at 2C. After 500 cycles, the PNF-Li|| $\text{LiFePO}_4$  maintains a reversible capacity of  $130.9 \text{ mAh g}^{-1}$  with a stable CE of 99.9% and capacity retention of 95.3%, while the NF-Li|| $\text{LiFePO}_4$  shows a lower capacity of  $125 \text{ mAh/g}$  with shorter cycling life of 350 cycles. When PNF-Li|| $\text{LiFePO}_4$  runs 1700 cycles, it keeps a reversible capacity of  $110.4 \text{ mAh g}^{-1}$  with a stable CE of 99.74% and a capacity retention of 80.3% at 2C (Fig. S15). Fig. 6(f) shows that the flat charge/discharge platforms of PNF-Li|| $\text{LiFePO}_4$  have lower voltage polarization ( $104.5 \text{ mV}$ ) than NF-Li|| $\text{LiFePO}_4$  ( $147.5 \text{ mV}$ ) (Fig. 6e). With the same testing conditions, the Li|| $\text{LiFePO}_4$  battery exhibits an obvious declining capacity of  $130.7 \text{ mAh g}^{-1}$  after 300 cycles at 1C (Fig. S16). In addition, PNF-Li|| $\text{LiFePO}_4$  full-cell possesses outstand-

ing rate performance than NF-Li|| $\text{LiFePO}_4$  in Fig. 6(d). The discharge capacity of PNF-Li|| $\text{LiFePO}_4$  could keep  $112.9 \text{ mAh g}^{-1}$  at 5C. When the rate is reduced again to 0.5C, a capacity of  $147.8 \text{ mAh g}^{-1}$  is recovered after 80 cycles without obvious attenuation. However, NF-Li|| $\text{LiFePO}_4$  represents obvious lower capacity at the same rate and poor rate performance. The improvement results of the full cell indicate that lithiophilic  $\text{Ni}_2\text{P}$  nanoarrays in-situ modified nickel foam is a stable 3D skeleton inducing the formation of a uniform and robust SEI, achieving the homogeneous Li plating/stripping.

### 3. Conclusions

In summary, a 3D conducting scaffold with in-situ grown lithiophilic  $\text{Ni}_2\text{P}$  nanoarrays has been well-designed via the facile two-step process of hydrothermal-phosphating. The lithiophilic  $\text{Ni}_2\text{P}$  nanoarrays with outstanding lithiophilicity, electrical conductivity and structural stability, which effectively increase specific surface area, lower local current density and reduce nucleation overpotential. Importantly, the in-situ formed passivation layer containing LiP/Li<sub>3</sub>P by the reaction of  $\text{Ni}_2\text{P}$  and Li provides more sites for lithium nucleation, conducting fast and uniform transfer of ions. In addition,  $\text{Ni}_2\text{P}$  with metalloid characteristics and in-situ formed nano Ni present superior conductivity contributing to improve electrochemical kinetics and realize Li uniform plating/stripping, then chronically suppressing the growth of Li dendrites and

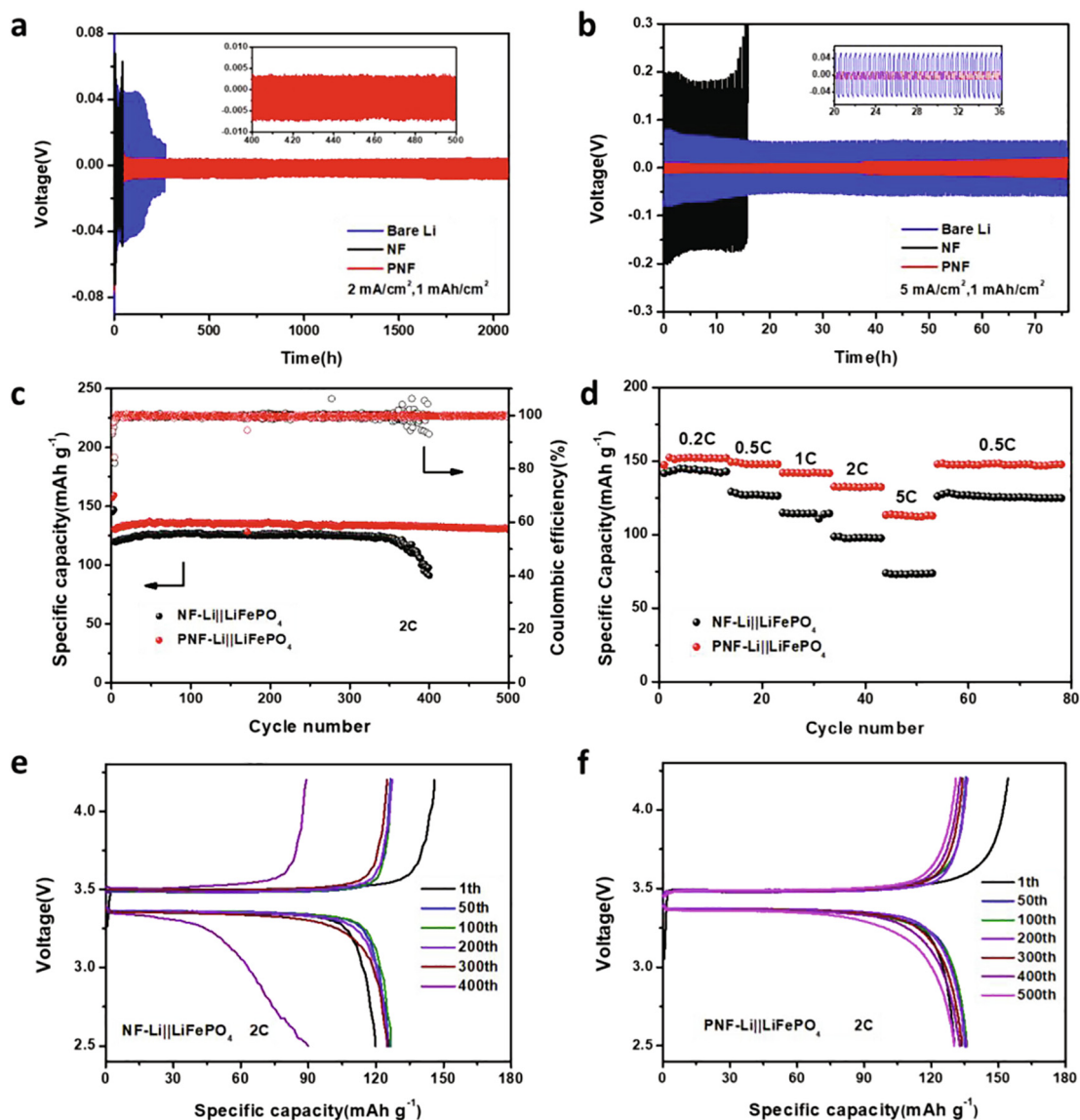


**Fig. 6.** Electrochemical performance of symmetric cells and full cells. Galvanostatic plating/stripping profiles in symmetric cells at a current density of (a) 2 mA cm<sup>-2</sup> and (b) 5 mA cm<sup>-2</sup> for 1 mAh cm<sup>-2</sup>; (c) cycling performance comparison between PNF-Li||LiFePO<sub>4</sub> and NF-Li||LiFePO<sub>4</sub> cell at 2C; (d) rate performance between PNF-Li||LiFePO<sub>4</sub> and NF-Li||LiFePO<sub>4</sub> cell. The charge/discharge profiles of NF-Li||LiFePO<sub>4</sub> (e) and PNF-Li||LiFePO<sub>4</sub> (f) at 2C.

volume change. Based on these advantages, a high Coulombic efficiency of 98% over 210 cycles at 3 mA cm<sup>-2</sup> and long lifespan of 2100 h over 2000 cycles with a low voltage hysteresis at 2 mA cm<sup>-2</sup> have been achieved. When paired with LiFePO<sub>4</sub> cathode, the full-cell with Li-plated PNF electrode shows a high reversible capacity of 130.9 mAh g<sup>-1</sup> with a stable CE of 99.9% and a capacity retention of 95.3% after 500 cycles at 2C. It maintains a capacity retention of 80.3% with a stable CE of 99.74% over 1700 cycles, and presents excellent rate performance. Furthermore, this work lights up nickel phosphide as lithiophilic layer for stable Li metal anodes, and provides a simple method of surface and structure regulation that can be promoted in catalysis, energy storage devices, and other fields.

### Supporting materials

Experimental details, including synthetic methods, characterization, electrochemical characterization and theoretical calculations.

In addition, mechanism of material preparation, BET, SEM images, XRD characterization, XPS characterization, EIS, CV, and additional electrochemical cycling data are provided (PDF).

### Declaration of Competing Interest

The authors declare that they have no known competing financial interests or personal relationships that could have appeared to influence the work reported in this paper.

### Acknowledgments

We appreciate financial supported by the National Natural Science Foundation of China (Grant Nos. 51874361 and 51904343), the Science and technology program of Hunan Province (2019RS3002).



## Appendix A. Supplementary data

Supplementary data to this article can be found online at <https://doi.org/10.1016/j.jechem.2020.06.004>.

## References

- [1] Z.P. Cano, D. Banham, S. Ye, A. Hintennach, J. Lu, M. Fowler, Z. Chen, *Nat. Energy* 3 (2018) 279–289.
- [2] W.A. Braff, J.M. Mueller, J.E. Trancik, *Nat. Clim. Chang.* 6 (2016) 964–969.
- [3] A. Mukhopadhyay, M.K. Jangid, *Science* 359 (2018) 1463.
- [4] P.G. Bruce, S.A. Freunberger, L.J. Hardwick, J. Tarascon, *Nat. Mater.* 11 (2012) 19–29.
- [5] Y. Liu, D. Lin, Z. Liang, J. Zhao, K. Yan, Y. Cui, *Nat. Commun.* 7 (2016) 12015.
- [6] W. Xu, J. Wang, F. Ding, X. Chen, E. Nasybutin, Y. Zhang, J. Zhang, *Energy Environ. Sci.* 7 (2014) 513–537.
- [7] R. Wang, W. Cui, F. Chu, F. Wu, *J. Energy Chem.* 48 (2020) 145–159.
- [8] X.Q. Zhang, X.B. Cheng, X. Chen, C. Yan, Q. Zhang, *Adv. Funct. Mater.* 27 (2017) 1605989.
- [9] F. Ding, W. Xu, G.L. Graff, J. Zhang, M.L. Sushko, X. Chen, Y. Shao, M.H. Engelhard, Z. Nie, J. Xiao, X. Liu, P.V. Sushko, J. Liu, J. Zhang, *J. Am. Chem. Soc.* 135 (2013) 4450–4456.
- [10] W. Li, H. Yao, K. Yan, G. Zheng, Z. Liang, Y. Chiang, Y. Cui, *Nat. Commun.* 6 (2015) 7436.
- [11] M. Zhu, J. Wu, Y. Wang, M. Song, L. Long, S.H. Siyal, X. Yang, G. Sui, *J. Energy Chem.* 37 (2019) 126–142.
- [12] Y.X. Yuan, F. Wu, G.H. Chen, Y. Bai, C. Wu, *J. Energy Chem.* 37 (2019) 197–203.
- [13] M. Ryou, Y.M. Lee, Y. Lee, M. Winter, P. Bieker, *Adv. Funct. Mater.* 25 (2015) 834–841.
- [14] K. Shen, B. Li, S. Yang, *Energy Storage Mater.* 24 (2020) 670–675.
- [15] X. Shen, X. Cheng, P. Shi, J. Huang, X. Zhang, C. Yan, T. Li, Q. Zhang, *J. Energy Chem.* 37 (2019) 29–34.
- [16] C. Brissot, M. Rosso, J.N. Chazalviel, P. Baudry, S. Lascaud, *Electrochim. Acta* 43 (1998) 1569–1574.
- [17] S. Ni, S. Tan, Q. An, L. Mai, *J. Energy Chem.* 44 (2020) 73–89.
- [18] K. Yan, Z. Lu, H. Lee, F. Xiong, P. Hsu, Y. Li, J. Zhao, S. Chu, Y. Cui, *Nat. Energy* 1 (2016) 16010.
- [19] H. Wang, Y. Li, Y. Li, Y. Liu, D. Lin, C. Zhu, G. Chen, A. Yang, K. Yan, H. Chen, Y. Zhu, J. Li, J. Xie, J. Xu, Z. Zhang, R. Vilá, A. Pei, K. Wang, Y. Cui, *Nano Lett.* 19 (2019) 1326–1335.
- [20] D. Lin, Y. Liu, Z. Liang, H. Lee, J. Sun, H. Wang, K. Yan, J. Xie, Y. Cui, *Nat. Nanotechnol.* 11 (2016) 626–632.
- [21] D. Kang, K. Tang, J. Koh, W. Liang, J.P. Lemmon, *J. Energy Chem.* 44 (2020) 68–72.
- [22] L. Kong, X. Fu, S. Qi, D. Wu, Y. Wang, W. Zhong, *Electrochim. Acta* 318 (2019) 220–227.
- [23] Y. Xu, A.S. Menon, P.P.R.M. Harks, D.C. Hermes, L.A. Haverkate, S. Unnikrishnan, F.M. Mulder, *Energy Storage Mater.* 12 (2018) 69–78.
- [24] W. Xi, G. Yan, Z. Lang, Y. Ma, H. Tan, H. Zhu, Y. Wang, Y. Li, *Small* 14 (2018) 1802204.
- [25] X. Xiong, D. Ding, D. Chen, G. Waller, Y. Bu, Z. Wang, M. Liu, *Nano Energy* 11 (2015) 154–161.
- [26] S. Lu, Z. Wang, H. Yan, R. Wang, K. Lu, Y. Cheng, W. Qin, X. Wu, *J. Energy Chem.* 41 (2020) 87–92.
- [27] Q. Li, S. Zhu, Y. Lu, *Adv. Funct. Mater.* 27 (2017) 1606422.
- [28] S. Chi, Y. Liu, W. Song, L. Fan, Q. Zhang, *Adv. Funct. Mater.* 27 (2017) 1700348.
- [29] H. Fan, C. Gao, H. Jiang, Q. Dong, B. Hong, Y. Lai, *J. Energy Chem.* 49 (2020) 59–70.
- [30] J. Pu, J. Li, K. Zhang, T. Zhang, C. Li, H. Ma, J. Zhu, P.V. Braun, J. Lu, H. Zhang, *Nat. Commun.* 10 (2019) 1896.
- [31] B. Hong, H. Fan, X. Cheng, X. Yan, S. Hong, Q. Dong, C. Gao, Z. Zhang, Y. Lai, Q. Zhang, *Energy Storage Mater.* 16 (2019) 259–266.
- [32] H. Fan, C. Gao, Q. Dong, B. Hong, Z. Fang, M. Hu, Y. Lai, *J. Electroanal. Chem.* 824 (2018) 175–180.
- [33] X. Yue, W. Wang, Q. Wang, J. Meng, X. Wang, Y. Song, Z. Fu, X. Wu, Y. Zhou, *Energy Storage Mater.* 21 (2019) 180–189.
- [34] C. Sun, Y. Li, J. Jin, J. Yang, Z. Wen, *J. Mater. Chem. A* 7 (2019) 7752–7759.
- [35] S. Huang, W. Zhang, H. Ming, G. Cao, L. Fan, H. Zhang, *Nano Lett.* 19 (2019) 1832–1837.
- [36] X. Yue, W. Wang, Q. Wang, J. Meng, Z. Zhang, X. Wu, X. Yang, Y. Zhou, *Energy Storage Mater.* 14 (2018) 335–344.
- [37] Z. Huang, C. Zhang, W. Lv, G. Zhou, Y. Zhang, Y. Deng, H. Wu, F. Kang, Q. Yang, *J. Mater. Chem. A* 7 (2019) 727–732.
- [38] J. Zhu, J. Chen, Y. Luo, S. Sun, L. Qin, H. Xu, P. Zhang, W. Zhang, W. Tian, Z. Sun, *Energy Storage Mater.* 23 (2019) 539–546.
- [39] X. Wang, Z. Pan, Y. Wu, G. Xu, X. Zheng, Y. Qiu, M. Liu, Y. Zhang, W. Li, *Nanoscale* 10 (2018) 16562–16567.
- [40] Q. Sun, W. Zhai, G. Hou, J. Feng, L. Zhang, P. Si, S. Guo, L. Ci, *ACS Sustain. Chem. Eng.* 6 (2018) 15219–15227.
- [41] G. Li, Z. Liu, Q. Huang, Y. Gao, M. Regula, D. Wang, L. Chen, D. Wang, *U.P.P.U. Nat. Energy* 3 (2018) 1076–1083.
- [42] C. Yang, Y. Yin, S. Zhang, N. Li, Y. Guo, *Nat. Commun.* 6 (2015) 8058.
- [43] K. Wu, B. Zhao, C. Yang, Q. Wang, W. Liu, H. Zhou, *J. Energy Chem.* 43 (2020) 16–23.
- [44] X. Liu, W. Li, X. Zhao, Y. Liu, C. Nan, L. Fan, *Adv. Funct. Mater.* 29 (2019) 1901510.
- [45] Q. Li, J. Ma, H. Wang, X. Yang, R. Yuan, Y. Chai, *Electrochim. Acta* 213 (2016) 201–206.
- [46] G. Yang, Y. Li, Y. Tong, J. Qiu, S. Liu, S. Zhang, Z. Guan, B. Xu, Z. Wang, L. Chen, *Nano Lett.* 19 (2019) 494–499.
- [47] G. Nazri, *Solid State Ion.* 34 (1989) 97–102.
- [48] C. Sun, A. Lin, W. Li, J. Jin, Y. Sun, J. Yang, Z. Wen, *Adv. Energy Mater.* 10 (2020) 1902989.
- [49] K.N. Wood, K.X. Steirer, S.E. Hafner, C. Ban, S. Santhanagopalan, S. Lee, G. Teeter, *Nat. Commun.* 9 (2018) 2490.
- [50] R. Reinhold, U. Stoeck, H. Grafe, D. Mikhailova, T. Jaumann, S. Oswald, S. Kaskel, L. Giebeler, *ACS Appl. Mater. Inter.* 10 (2018) 7096–7106.
- [51] L. Lin, F. Liang, K. Zhang, H. Mao, J. Yang, Y. Qian, *J. Mater. Chem. A* 6 (2018) 15859–15867.
- [52] Y. Feng, H. Zhang, Y. Mu, W. Li, J. Sun, K. Wu, Y. Wang, *Chem.-Eur. J.* 21 (2015) 9229–9235.
- [53] C. Villevieille, F. Robert, P.L. Taberna, L. Bazin, P. Simon, L. Monconduit, *J. Mater. Chem.* 18 (2008) 5956–5960.
- [54] X. Cheng, C. Yan, X. Zhang, H. Liu, Q. Zhang, *ACS Energy Lett.* 3 (2018) 1564–1570.
- [55] H. Zhang, X. Liao, Y. Guan, Y. Xiang, M. Li, W. Zhang, X. Zhu, H. Ming, L. Lu, J. Qiu, Y. Huang, G. Cao, Y. Yang, L. Mai, Y. Zhao, H. Zhang, *Nat. Commun.* 9 (2018) 3729.
- [56] C. Zhao, P. Chen, R. Zhang, X. Chen, B. Li, X. Zhang, X. Cheng, Q. Zhang, *Sci. Adv.* 4 (2018) eaat3446.